Strain Quantum Sensing with Spin Defects in Hexagonal Boron Nitride

Xiaodan Lyu, Qinghai Tan, Lishu Wu, Chusheng Zhang, Zhaowei Zhang, Zhao Mu, Jesús Zúñiga-Pérez, Hongbing Cai, Weibo Gao

Strain quantum sensing with spin defects in hexagonal boron nitride

Xiaodan Lyu,[†,⊥] Qinghai Tan,[†] Lishu Wu,[†] Chusheng Zhang,[†] Zhaowei Zhang,[†] Zhao Mu,[†] Jesús Zúñiga-Pérez,[*,†,Ø] Hongbing Cai[*,†] and Weibo Gao[*,†,⊥]

[†]Division of Physics and Applied Physics, School of Physical and Mathematical Sciences, Nanyang Technological University, 637371, Singapore

[Ø] MajuLab, International Research Laboratory IRL 3654, CNRS, Université Côte d'Azur, Sorbonne Université, National University of Singapore, Nanyang Technological University, Singapore, Singapore

[⊥]The Photonics Institute and Centre for Disruptive Photonic Technologies, Nanyang Technological University, 637371, Singapore

Xiaodan Lyu: ID: orcid.org/0000-0003-1452-6620

Qinghai Tan: ID: orcid.org/0000-0003-4808-4795

[*] Jesús Zúñiga-Pérez: jesus.zuniga@ntu.edu.sg ID: orcid.org/0000-0002-7154-641X

[*] Hongbing Cai: richard.cai@ntu.edu.sg ID: orcid.org/0000-0003-3186-1041

[*] Weibo Gao: wbgao@ntu.edu.sg ID: orcid.org/0000-0003-3971-621X

Keywords: hexagonal boron nitride, strain, color center, optically detected magnetic resonance, Raman spectroscopy

Abstract: *Hexagonal boron nitride is not only a promising functional material for the development of 2-dimensional optoelectronic devices but also a good candidate for quantum sensing thanks to the presence of quantum emitters in the form of atom-like defects. Their exploitation in quantum technologies necessitates understanding their coherence properties as well as their sensitivity to external stimuli. In this work we probe the strain configuration of boron vacancy centers (VB^-) created by ion implantation in h-BN flakes thanks to wide field spatially-resolved optically detected magnetic resonance and sub-micro Raman spectroscopy. Our experiments demonstrate the ability of VB^- for quantum sensing of strain and, given the omnipresence of h-BN in 2D-based devices, open the door for in-situ imaging of strain under working conditions.*

Quantum sensing based on spin defects in wide band-gap semiconductors has seen a rapid development over the last fifteen years. Well-established quantum sensors, such as the NV^- center in diamond or spin defects in silicon carbide (SiC), have well-defined qubit levels and

can be initialized and read out optically.[1-5] They have laid the groundwork for high sensitivity quantum sensing.[6] The sensitivity of quantum sensors depends strongly on the distance between the spin-defect and the sensing target. Unfortunately, it is very challenging to generate near-surface color centers in those materials, which limits their interaction with external stimuli[7, 8] and, thus, does not allow to exploit their full potentiality. A solution for this challenge may be given by the van der Waals crystal hexagonal boron nitride (h-BN). In the context of quantum sensing h-BN presents several assets, as it can be easily exfoliated down to a few layers[9] and it can display spin defects near its surface, which can be created by a number of different approaches.[10-13] Among these defects, the negatively-charged boron vacancy center (VB^-) has received increasing attention in the last two years due to the ability to initialize and read-out its spin[11], and the possibility of establishing a coherent control of an ensemble of VB^-.

Importantly, h-BN is exploited today in almost every optoelectronic device and heterostructure comprising 2D crystals; it is used as a disorder-free substrate[14] as well as a dielectric material, which isolates the system from its environment and enhances thereby the electronic and optical figures of merit, including electronic mobility and quantum yield.[15, 16] Since h-BN inevitably interacts mechanically with the materials conforming the structure, understanding and characterizing the effect of strain on color centers in h-BN, in particular on VB^-, would open the door to monitor locally the strain of van der Waals heterostructures. Furthermore, because of the subtle interlayer interactions that govern sliding in 2D materials[17] a complete strain picture, i.e. in-plane and out-of-plane strain, would be desirable.

In this work we perform wide field spatially-resolved optically detected magnetic resonance (ODMR) spectroscopy on VB^-, combined with Raman imaging and second harmonic generation (SHG), to characterize the strain-spin coupling in VB^- and determine thereby both the in-plane and out-of-plane strain values. Note that combining ODMR and Raman spectroscopy is essential to uncouple the in-plane and out-of-plane strain contributions. Our study paves the way to utilize the flexible material h-BN as a tool for quantum sensing and information processing.

The negatively charged boron vacancy center (VB^-) consists of a boron vacancy with three adjacent nitrogen atoms in 2-dimensional h-BN[11, 18-20], as illustrated in Figure 1a. Boron defects in h-BN can be generated by ion implantation[21], electron irradiation[22], and femtosecond laser writing.[23] The energy levels of VB^- centers in the absence of external fields are shown in Figure

1b. It has a spin triplet ground state, which can be addressed and manipulated by microwaves, with a ground state zero-field splitting $D/h = 3.469$ GHz between the spin sublevels $m_s = 0$ and $m_s = \pm 1$. Once being excited, the VB^- center has two paths to decay: the radiative transition that will produce a PL around 850 nm as well as the non-radiative intersystem crossing.[24] Figure 1c shows a typical photoluminescence emission of an ensemble of VB^- centers at room temperature.

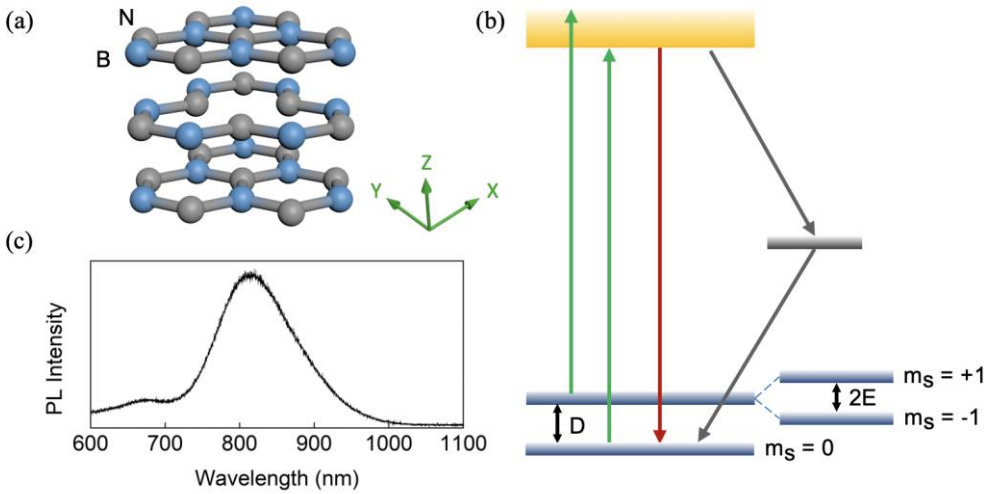

Figure 1. (a) Schematic drawing of VB^- center in h-BN denoting the coordinate axes. The h-BN symmetry axis defines the z direction. Blue: Boron atoms; Grey: Nitrogen atoms. (b) Diagram of VB^- center energy levels denoting the triplet ground state, whose energy levels are characterized by parameters D and E (see main text). (c) Photoluminescence spectrum of the sample at room temperature.

Its ODMR shows two resonant dips, associated to a decrease of fluorescence, that correspond to the transitions between $m_s = 0$ and $m_s = \pm 1$ spin sublevels (Figure 2c). The frequency at the center of these two dips is the zero-filed splitting frequency, while the degeneracy of the $m_s = \pm 1$ state can be lifted by non-zero strain or magnetic field, and is quantified by E.[25-28] To analyze the effect of strain in the VB^- energy level configuration we considered the D_{3h} symmetry for h-BN VB^- defects and obtained the general symmetry-allowed spin strain interaction Hamiltonian [26, 27, 29, 30], which has the form:

$$H_\varepsilon = H_{\varepsilon 0} + H_{\varepsilon 1} \quad (1)$$

$$H_{\varepsilon 0} = \left[a\left(\varepsilon_{xx} + \varepsilon_{yy}\right) + b\varepsilon_{zz}\right]S_z^2 \quad (2)$$

$$H_{\varepsilon 1} = \left[\frac{c}{2}\left(\varepsilon_{xx} - \varepsilon_{yy}\right)\right]\left(S_y^2 - S_x^2\right) + c\varepsilon_{xy}\left(S_xS_y + S_yS_x\right) \quad (3)$$

where $\boldsymbol{S} = \sum_{i=x,y,z} S_i$ is the total spin operator, a, b, c are the coupling-strength parameters between the spin and local strain, and $\boldsymbol{\varepsilon}$ is the strain tensor. The coordinates refer to the Cartesian $\{xyz\}$ axes defined in Figure 1a, with z aligned along the symmetry axis of the VB^- center, and (x,y) being in the h-BN flake plane. In the absence of external magnetic field, the spin resonances are given by

$$h\omega = D + D_S \pm \sqrt{E^2 + E_S^2} \tag{4}$$

$$D_S = \left[a\left(\varepsilon_{xx} + \varepsilon_{yy}\right) + b\varepsilon_{zz}\right]S_z^2 \tag{5}$$

$$E_S = \sqrt{\left[\frac{c}{2}\left(\varepsilon_{xx} - \varepsilon_{yy}\right)\right]^2 + (c\varepsilon_{xy})^2} \tag{6}$$

For our sample, the zero field parameters are $D/h = 3.469\ \mathrm{GHz}$ and $E/h = 68\ \mathrm{MHz}$, respectively, where h is Planck's constant. Here we obtain D and E from the results in the sample area without bubbles. Note that the E parameter is strongly sensitive on the implantation species and implantation conditions[25], the current E value being different from that in other samples where we have used Ga ions for creating the VB^- defects[20], instead of silicon as in the current sample. The effect of the different strain components on spin resonances can be seen from above equations. The effect of an out-of-plane strain, ε_{zz}, is equivalent to a pure D_S shift, modifying just the energy separation between the $m_s = 0$ and $m_s = \pm 1$ spin sublevels. On the other hand, the in-plane strain does not only affect this separation but also mixes the new eigenstates $\tilde{S}_x$ and $\tilde{S}_y$ and modify their energy separation.

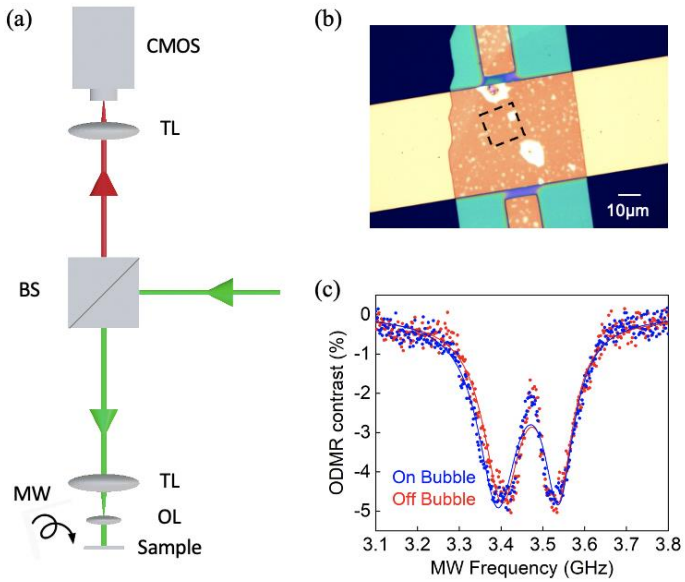

Figure 2. (a) *Schematic illustration of the spatially-resolved wide field imaging setup. TL: tube*

lens. DM: dichroic mirror. OL: objective lens. MW: microwave. BS: beam splitter. (b) Microscope image of the exfoliated h-BN lying on top of the microwave antenna. The area indicated with the dashed line is the investigated area in Figures 3 and 4. (c) Zero field ODMR spectra corresponding to locations on (blue) and off (red) bubbles. The solid lines show the fitting results.

To characterize the strain state around VB^- centers we deposited first a 50 μm large gold stripline on Si/SiO_2 substrate, which was used to deliver microwaves to the VB^- centers. Then, we transferred tape-exfoliated h-BN thereon. The optical microscopy image of the h-BN flake, 133±2 monolayers thick (see Supplementary Information), deposited on the microwave stripline is shown in Figure 2b. A large number of bubbles (bright spots in Figure 2b) were generated during the deposition process, as often found in reports on transferred 2D materials[31], and were intentionally not removed by any post-processing (or pre-cleaning of the stripline), as they will be exploited to illustrate the strain sensitivity enabled by ODMR. The bubbles generated during the transfer process are typically 10nm to 40nm high, and 1μm to 4μm large (see Supplementary Information for the atomic force microscopy images of bubbles 1 and 2 in Figure 3a), leading to much smaller strains than in voluntarily created bubbles.[32, 33] Note that since the bubbles in Figures 2b and 3a are not necessarily gas-filled, but can be created by particles remaining on the stripline before the h-BN transfer, their form does not necessarily show spherical or radial symmetry (e.g. bubble1, which displays a triangular pyramidal form). Finally, Si ions were used to implant h-BN nanosheets and create VB^- centers.

Before we probe the spin-strain interaction in VB^- centers we will first discuss spatially-resolved Raman measurements, which provide the in-plane strain distribution in the h-BN flake. Determining the in-plane strain distribution independently of ODMR measurements is crucial to access the out-of-plane strain thanks to the measurement of D_S (see Eq. (5)), otherwise one needs to make assumptions on the actual strain distribution.[34] Raman spectroscopy is a common method to explore strain by inspecting phonon vibration modes, among which E_{2g} is an in-plane Raman active mode at the Γ point.[32, 35-37] We chose two bubbles with different sizes and one flat area to evaluate the magnitude of strains (Figure 3a). As illustrated in Figure 3b, the spectrum of the unstrained area shows a peak at $1366.3 \pm 0.7\ \mathrm{cm}^{-1}$, which is consistent with the reported bulk h-BN flake.[37] The E_{2g} signals show a redshift of $1.0\ \mathrm{cm}^{-1}$ and $1.5\ \mathrm{cm}^{-1}$ for bubble1 and bubble2, respectively. This redshift represents a tensile strain on the bubbles.

The relative Raman shift of a line cut along the diameter of bubble2 is depicted in Figure 3c; the magnitude of in-plane strain attains its maximum at the bubble summit. There is no Raman shift at the edge of the bubbles, implying that in-plane strain is negligible. For the E_{2g} mode, the frequency shift is linearly dependent on external strains,[36] with a shift rate $\Delta = -\partial\omega/\partial\varepsilon_{in}$ under in-plane strain $\varepsilon_{in} = \varepsilon_{xx} + \varepsilon_{yy}$ equal to 27.9 $\mathrm{cm}^{-1}/\%$, which has been determined by previous reports analyzing the vibration response of h-BN sheets to external strain.[32] We performed Raman mapping on a $15\mu\mathrm{m} \times 15\mu\mathrm{m}$ area (Figure 3a) by recording the Raman spectrum for each $348n\mathrm{m} \times 348n\mathrm{m}$ pixel. Automatic Lorentz fitting was done to determine the peak position for each spectrum, while the Raman frequency probed on flat regions was used to calculate the Raman shift (see supplementary information). In this way, we obtain the total in-plane strain maps of our sample (Figure 3d), which shows that E_{2g} peak redshifts to lower wavelength on h-BN bubbles.

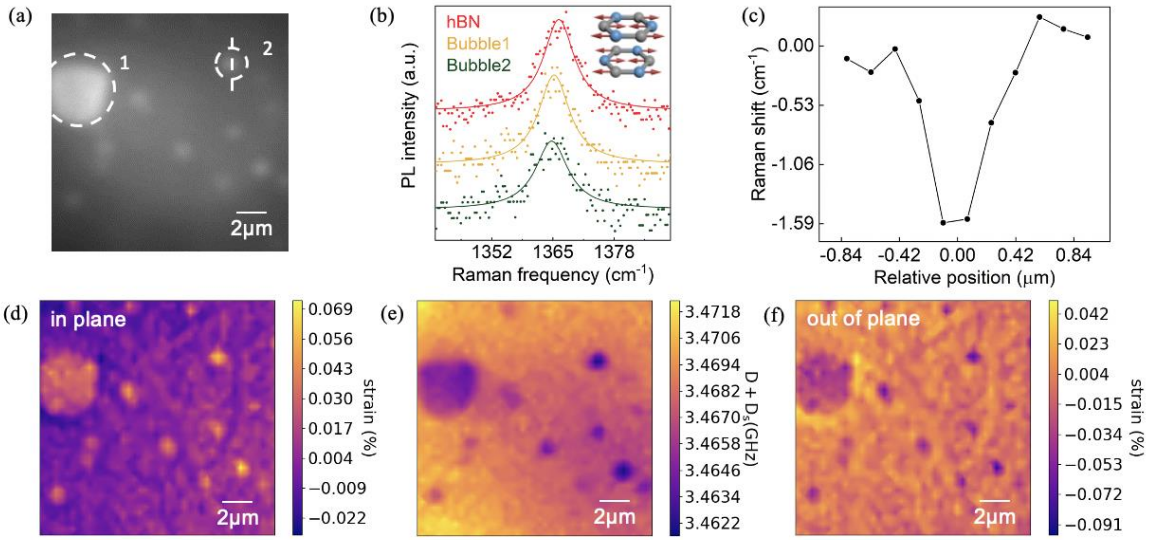

Figure 3. (a) Bright-field optical microscopy image of h-BN bubbles in the $15\mu m \times 15\mu m$ *area of interest. (b) Raman spectra corresponding to on (yellow and green) and off (red) h-BN bubbles. Inset: schematic drawing of phonon vibrations corresponding to* E_{2g} *mode. The arrows indicate directions of atom motions. (c) Raman frequency shift as a function of the position along the diameter of bubble2 indicated in a. (d) The strain maps of in-plane strain* ε_{in} *distribution within the area in a. (e) ODMR parameters corresponding to the shift* $D + D_S$*. (f) The strain map of out-of-plane strain within the area in a.*

To access the out-of-plane strain we analyze the VB^- spin resonances by performing continuous wave ODMR with a home-built spatially-resolved wide field setup (Figure 2a). A 532nm laser

was focused on the objective's back focal plane to create a wide field illumination of the sample. Photoluminescence from the VB^- centers was collected and imaged with a camera. According to Eq. (5), the strain-dependent contribution to the zero-field splitting D_S depends on the local normal strains $\varepsilon_{xx}, \varepsilon_{yy}, \varepsilon_{zz}$ and, thus, its measurement enables to determine the out-of-plane strain, provided the total in-plane strain is known independently. A map of the zero-field splitting term $D + D_S$ is depicted in Figure 3e, indicating a splitting between $m_s = 0$ and $m_s = \pm 1$ spin sublevels that reaches its maximum at the summit of the small "bubbles". To determine the out-of-plane strain distribution we use Eq. (5) with $a = -40.5\text{GHz}$ and $b = -24.5\text{GHz}$, as recently determined by temperature dependent ODMR measurements on VB^- centers,[19] and make use of the in-plane strain map measured by Raman mapping (figure 3d). The out-of-plane strain distribution ε_{zz} obtained thereby is shown in Figure 3f, which corresponds thus to the subtraction of figure 3(d) from figure 3(e) through Eq. (5), weighted by parameters a and b. The sign of the out-of-plane strain is negative on the bubbles, implying that the spacing between adjacent h-BN layers in the flake decreases. For the studied h-BN flake, which is 43.9±0.5nm thick, the compression of the *c* lattice parameter is roughly three times larger than the expansion of the in-plane *a* lattice parameter, and, thus, cannot be neglected.[34] The out-of-plane/total in-plane strain ratio amounts to $\nu = 1.32 \pm 0.2$, which was extracted from the strain values measured in the smallest and radially symmetric bubbles (i.e. on those displaying the same geometry as bubble2).

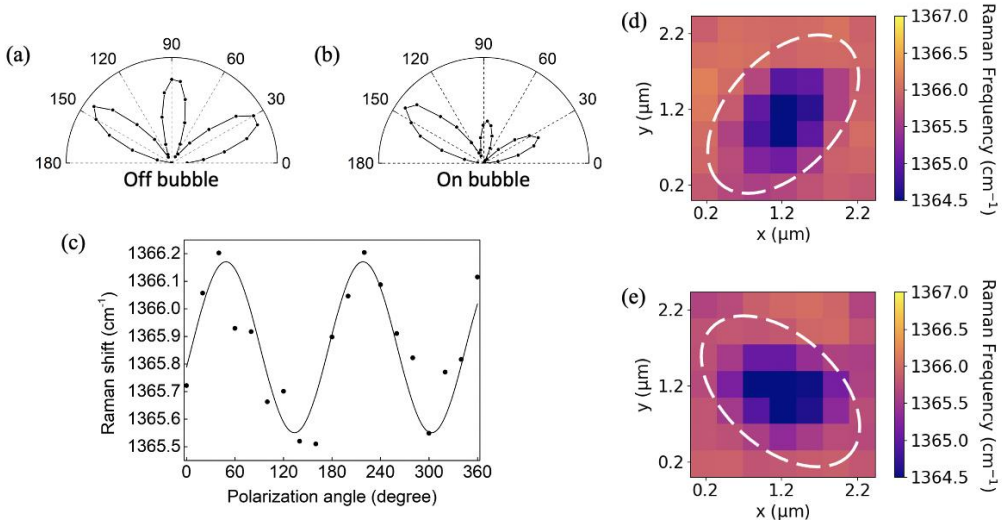

Figure 4. (a) and (b) Linear polarization resolved SHG intensity from flat areas and h-BN bubbles. (c) Shift of Raman frequency as a function of sample rotation angle. Lines: fitting results with sine function. (d) and (e) The Raman frequency map of bubble2 with polarization angle fixed at $120°$*(d) and* $30°$*(e). The size of each pixel is* $348nm \times 348nm$.

Besides the normal local strains, we need to assess the potential anisotropy of in-plane strain and the presence of shear strains. SHG is a process by which two photons at frequency ω are converted into a photon of 2ω frequency.[38-40] The correspondence between SHG intensity and pump electric field is defined by the second-order nonlinear susceptibility tensor $\chi_{ijk}^{(2)}$, which is linearly related to the strain tensor through the fifth-rank photoeleastic tensor.[38, 39] Upon knowledge of the independent components of the photoeleastic tensor corresponding to h-BN, one could in principle retrieve the spatially-resolved in-plane anisotropy by acquiring several polarization-resolved SHG images.[38] In the current work we aim to use SHG, as well as polarization-resolved Raman spectroscopy[32], to show qualitatively that an in-plane anisotropy exists. The polarization resolved SHG from the h-BN flake within a flat region with a pump laser wavelength at 880 nm uncovers its six-fold lattice symmetry (Figure 4a). Due to lattice deformation, polarization-resolved SHG measured on bubbles display asymmetric intensity distributions (Figure 4b), which point towards an anisotropic strain distribution on the bubbles, that is, $\varepsilon_{xx} \neq \varepsilon_{yy}$. We further confirmed it with polarized Raman spectroscopy that, when performed on a bubble, displays a periodic shift of the center-of-mass Raman frequency, between $1365.5\ \mathrm{cm}^{-1}$ and $1366.2\ \mathrm{cm}^{-1}$, when changing the polarization angle (Figure 4c). This periodic shift is due to the coexistence of two strain-split but unresolved Raman $\mathrm{E_{2g}}$ modes that attest of a strain anisotropy in the bubbles, with the two modes being in counterphase (see Figures 4d and 4e).[32] These measurements show qualitatively the presence of an anisotropic strain.

To quantify the strain anisotropy, we make use of the strain-dependent $\mathrm{E_S}$ parameter extracted from the ODMR measurements, see Eq. (6), and map its value in the region of interest (Figure 5a). Indeed, within the bubbles and with the assumptions of spherical symmetry and relatively small deformations, the term $\mathrm{E_S}$ in Eq. (6) can be rewritten in polar coordinates (see Supplementary Information) as

$$E_S = \frac{c}{2}(\varepsilon_{rr} - \varepsilon_{\theta\theta}) \tag{7}$$

where ε_{rr} and $\varepsilon_{\theta\theta}$ represent the radial and circumferential in-plane strain components in polar coordinates. As shown in the zoom images (Figures 5(b) and (c)), the strain anisotropy evidenced by a nonzero $\mathrm{E_S}$ value is non-negligible in the bubbles. This asymmetric strain distribution might be related to the origin of our bubbles, which are created by the h-BN lying on top of microparticles and not by gas trapping.[31] Finally note that in order to give a

quantitative estimation of the shear strain one would need to know the value of the *c* parameter for h-BN, which needs to be investigated in future research with controllable strain.

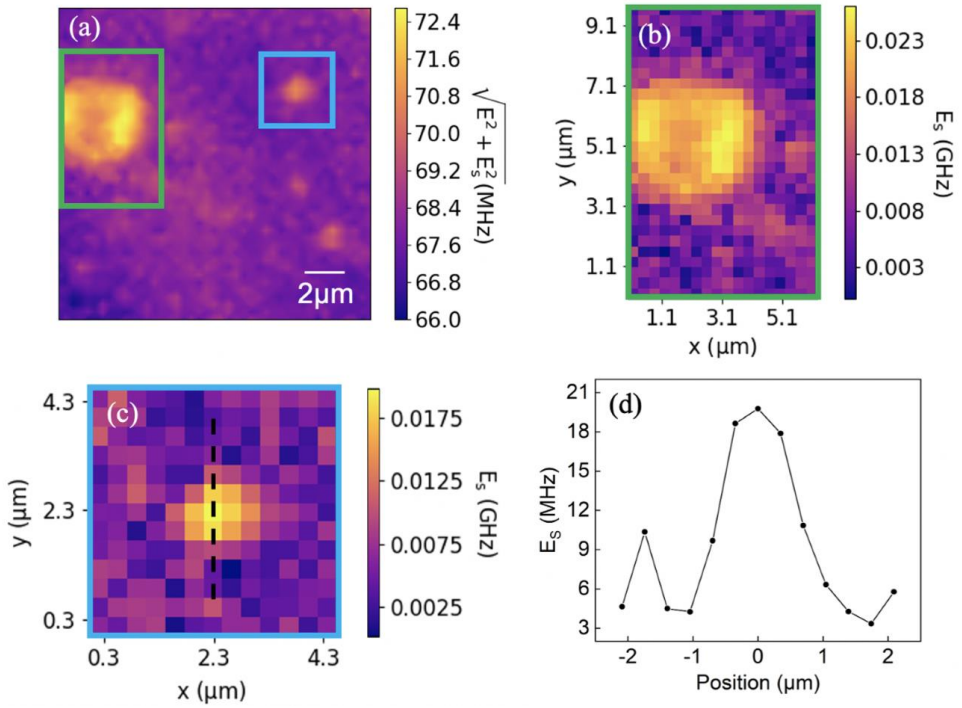

Figure 5. (a) ODMR $\sqrt{E^2 + E_S^2}$ *parameter corresponding to half the splitting between sublevels* $m_s = \pm 1$*, and representing the in-plane shear strain. (b) and (c)* E_S *parameter measured around bubbles 1 and 2, respectively. (d) Line scan through the dashed line in (c).*

To summarize, we analyzed the full strain distribution, i.e. in-plane and out-of-plane, in h-BN flakes thanks to the combination of spatially-resolved Raman and ODMR spectroscopies. From Raman measurements of the E_{2g} phonon vibration we extracted the total in-plane strain, which is tensile on the bubbles formed during the transfer process and reaches its maximum at the summit of the bubbles. The ODMR measurement of VB^- centers gives access to the strain along the out-of-plane direction, revealing a decrease of the spacing between adjacent h-BN layers in the bubbles. Finally, from the ODMR measurement of the spin $m_s = \pm 1$ sublevels separation we have been able to map the in-plane strain anisotropy, providing for the first time a full strain map around color centers in h-BN. Since h-BN is used as substrate and/or dielectric and/or protection layer in most 2D-based heterostructures, the technique and methodology introduced in this paper promotes h-BN as a sensor to measure *in-situ* the strain status of complex 2D materials stacks.[41] Besides, due to its unique mechanical properties and low cost compared to other existing quantum sensors, such as nitrogen vacancy centers in diamond, VB^- in h-BN can begin to be considered as a realistic platform for quantum sensing[42].

Supporting Information

Methods on sample preparation, ODMR, Raman spectroscopy, Second harmonic generation and deviation of spin mechanical interaction Hamiltonian, data analysis on Raman and ODMR, AFM analysis of bubbles and h-BN flakes, Raman analysis for the bubble.

Acknowledgments

REFERENCES

1. Doherty, M. W.; Struzhkin, V. V.; Simpson, D. A.; McGuinness, L. P.; Meng, Y.; Stacey, A.; Karle, T. J.; Hemley, R. J.; Manson, N. B.; Hollenberg, L. C. L.; Prawer, S., Electronic Properties and Metrology Applications of the Diamond ${\mathrm{NV}}^{\ensuremath{-}}$ Center under Pressure. *Physical Review Letters* **2014,** *112* (4), 047601.

2. Kucsko, G.; Maurer, P. C.; Yao, N. Y.; Kubo, M.; Noh, H. J.; Lo, P. K.; Park, H.; Lukin, M. D., Nanometre-scale thermometry in a living cell. *Nature* **2013,** *500* (7460), 54-58.

3. Maze, J. R.; Stanwix, P. L.; Hodges, J. S.; Hong, S.; Taylor, J. M.; Cappellaro, P.; Jiang, L.; Dutt, M. V. G.; Togan, E.; Zibrov, A. S.; Yacoby, A.; Walsworth, R. L.; Lukin, M. D., Nanoscale magnetic sensing with an individual electronic spin in diamond. *Nature* **2008,** *455* (7213), 644-647.

4. Bucher, D. B.; Aude Craik, D. P. L.; Backlund, M. P.; Turner, M. J.; Ben Dor, O.; Glenn, D. R.; Walsworth, R. L., Quantum diamond spectrometer for nanoscale NMR and ESR spectroscopy. *Nature Protocols* **2019,** *14* (9), 2707-2747.

5. Zhou, Y.; Wang, J.; Zhang, X.; Li, K.; Cai, J.; Gao, W., Self-Protected Thermometry with Infrared Photons and Defect Spins in Silicon Carbide. *Physical Review Applied* **2017,** *8* (4), 044015.

6. Barry, J. F.; Schloss, J. M.; Bauch, E.; Turner, M. J.; Hart, C. A.; Pham, L. M.; Walsworth, R. L., Sensitivity optimization for NV-diamond magnetometry. *Reviews of Modern Physics* **2020,** *92* (1), 015004.

7. Pham, L. M.; DeVience, S. J.; Casola, F.; Lovchinsky, I.; Sushkov, A. O.; Bersin, E.; Lee, J.; Urbach, E.; Cappellaro, P.; Park, H.; Yacoby, A.; Lukin, M.; Walsworth, R. L., NMR technique for determining the depth of shallow nitrogen-vacancy centers in diamond. *Physical Review B* **2016,** *93* (4), 045425.

8. Tetienne, J. P.; de Gille, R. W.; Broadway, D. A.; Teraji, T.; Lillie, S. E.; McCoey, J. M.; Dontschuk, N.; Hall, L. T.; Stacey, A.; Simpson, D. A.; Hollenberg, L. C. L., Spin properties of dense near-surface ensembles of nitrogen-vacancy centers in diamond. *Physical Review B* **2018,** *97* (8), 085402.

9. Caldwell, J. D.; Aharonovich, I.; Cassabois, G.; Edgar, J. H.; Gil, B.; Basov, D. N., Photonics with hexagonal boron nitride. *Nature Reviews Materials* **2019,** *4* (8), 552-567.

10. Shotan, Z.; Jayakumar, H.; Considine, C. R.; Mackoit, M.; Fedder, H.; Wrachtrup, J.; Alkauskas, A.; Doherty, M. W.; Menon, V. M.; Meriles, C. A., Photoinduced Modification of Single-Photon Emitters in Hexagonal Boron Nitride. *ACS Photonics* **2016,** *3* (12), 2490-2496.

11. Gottscholl, A.; Kianinia, M.; Soltamov, V.; Orlinskii, S.; Mamin, G.; Bradac, C.; Kasper, C.; Krambrock, K.; Sperlich, A.; Toth, M.; Aharonovich, I.; Dyakonov, V., Initialization and

read-out of intrinsic spin defects in a van der Waals crystal at room temperature. *Nature Materials* **2020,** *19* (5), 540-545.
12. Fournier, C.; Plaud, A.; Roux, S.; Pierret, A.; Rosticher, M.; Watanabe, K.; Taniguchi, T.; Buil, S.; Quélin, X.; Barjon, J.; Hermier, J.-P.; Delteil, A., Position-controlled quantum emitters with reproducible emission wavelength in hexagonal boron nitride. *Nature Communications* **2021,** *12* (1), 3779.
13. Grosso, G.; Moon, H.; Lienhard, B.; Ali, S.; Efetov, D. K.; Furchi, M. M.; Jarillo-Herrero, P.; Ford, M. J.; Aharonovich, I.; Englund, D., Tunable and high-purity room temperature single-photon emission from atomic defects in hexagonal boron nitride. *Nature Communications* **2017,** *8* (1), 705.
14. Dean, C. R.; Young, A. F.; Meric, I.; Lee, C.; Wang, L.; Sorgenfrei, S.; Watanabe, K.; Taniguchi, T.; Kim, P.; Shepard, K. L.; Hone, J., Boron nitride substrates for high-quality graphene electronics. *Nature Nanotechnology* **2010,** *5* (10), 722-726.
15. Mayorov, A. S.; Gorbachev, R. V.; Morozov, S. V.; Britnell, L.; Jalil, R.; Ponomarenko, L. A.; Blake, P.; Novoselov, K. S.; Watanabe, K.; Taniguchi, T.; Geim, A. K., Micrometer-Scale Ballistic Transport in Encapsulated Graphene at Room Temperature. *Nano Letters* **2011,** *11* (6), 2396-2399.
16. Hunt, B.; Sanchez-Yamagishi, J. D.; Young, A. F.; Yankowitz, M.; LeRoy, B. J.; Watanabe, K.; Taniguchi, T.; Moon, P.; Koshino, M.; Jarillo-Herrero, P.; Ashoori, R. C., Massive Dirac Fermions and Hofstadter Butterfly in a van der Waals Heterostructure. *Science* **2013,** *340* (6139), 1427-1430.
17. Falin, A.; Cai, Q.; Santos, E. J. G.; Scullion, D.; Qian, D.; Zhang, R.; Yang, Z.; Huang, S.; Watanabe, K.; Taniguchi, T.; Barnett, M. R.; Chen, Y.; Ruoff, R. S.; Li, L. H., Mechanical properties of atomically thin boron nitride and the role of interlayer interactions. *Nature Communications* **2017,** *8* (1), 15815.
18. Gao, X.; Jiang, B.; Llacsahuanga Allcca, A. E.; Shen, K.; Sadi, M. A.; Solanki, A. B.; Ju, P.; Xu, Z.; Upadhyaya, P.; Chen, Y. P.; Bhave, S. A.; Li, T., High-Contrast Plasmonic-Enhanced Shallow Spin Defects in Hexagonal Boron Nitride for Quantum Sensing. *Nano Letters* **2021,** *21* (18), 7708-7714.
19. Gottscholl, A.; Diez, M.; Soltamov, V.; Kasper, C.; Krauße, D.; Sperlich, A.; Kianinia, M.; Bradac, C.; Aharonovich, I.; Dyakonov, V., Spin defects in hBN as promising temperature, pressure and magnetic field quantum sensors. *Nature Communications* **2021,** *12* (1), 4480.
20. Mu, Z.; Cai, H.; Chen, D.; Kenny, J.; Jiang, Z.; Ru, S.; Lyu, X.; Koh, T. S.; Liu, X.; Aharonovich, I.; Gao, W., Excited-State Optically Detected Magnetic Resonance of Spin Defects in Hexagonal Boron Nitride. *Physical Review Letters* **2022,** *128* (21), 216402.
21. Kianinia, M.; White, S.; Fröch, J. E.; Bradac, C.; Aharonovich, I., Generation of Spin Defects in Hexagonal Boron Nitride. *ACS Photonics* **2020,** *7* (8), 2147-2152.
22. Liu, W.; Li, Z.-P.; Yang, Y.-Z.; Yu, S.; Meng, Y.; Wang, Z.-A.; Li, Z.-C.; Guo, N.-J.; Yan, F.-F.; Li, Q.; Wang, J.-F.; Xu, J.-S.; Wang, Y.-T.; Tang, J.-S.; Li, C.-F.; Guo, G.-C., Temperature-Dependent Energy-Level Shifts of Spin Defects in Hexagonal Boron Nitride. *ACS Photonics* **2021,** *8* (7), 1889-1895.
23. Gao, X.; Pandey, S.; Kianinia, M.; Ahn, J.; Ju, P.; Aharonovich, I.; Shivaram, N.; Li, T., Femtosecond Laser Writing of Spin Defects in Hexagonal Boron Nitride. *ACS Photonics* **2021,** *8* (4), 994-1000.
24. Reimers, J. R.; Shen, J.; Kianinia, M.; Bradac, C.; Aharonovich, I.; Ford, M. J.; Piecuch, P., Photoluminescence, photophysics, and photochemistry of the

${{\mathrm{V}}_{\mathrm{B}}}^{\ensuremath{-}}$ defect in hexagonal boron nitride. *Physical Review B* **2020,** *102* (14), 144105.
25. Guo, N.-J.; Liu, W.; Li, Z.-P.; Yang, Y.-Z.; Yu, S.; Meng, Y.; Wang, Z.-A.; Zeng, X.-D.; Yan, F.-F.; Li, Q.; Wang, J.-F.; Xu, J.-S.; Wang, Y.-T.; Tang, J.-S.; Li, C.-F.; Guo, G.-C., Generation of Spin Defects by Ion Implantation in Hexagonal Boron Nitride. *ACS Omega* **2022,** *7* (2), 1733-1739.
26. Udvarhelyi, P.; Shkolnikov, V. O.; Gali, A.; Burkard, G.; Pályi, A., Spin-strain interaction in nitrogen-vacancy centers in diamond. *Physical Review B* **2018,** *98* (7), 075201.
27. Hughes, A. E.; Runciman, W. A., Uniaxial stress splitting of doubly degenerate states of tetragonal and trigonal centres in cubic crystals. *Proceedings of the Physical Society* **1967,** *90* (3), 827-838.
28. Teissier, J.; Barfuss, A.; Appel, P.; Neu, E.; Maletinsky, P., Strain Coupling of a Nitrogen-Vacancy Center Spin to a Diamond Mechanical Oscillator. *Physical Review Letters* **2014,** *113* (2), 020503.
29. Ivády, V.; Simon, T.; Maze, J. R.; Abrikosov, I. A.; Gali, A., Pressure and temperature dependence of the zero-field splitting in the ground state of NV centers in diamond: A first-principles study. *Physical Review B* **2014,** *90* (23), 235205.
30. Doherty, M. W.; Dolde, F.; Fedder, H.; Jelezko, F.; Wrachtrup, J.; Manson, N. B.; Hollenberg, L. C. L., Theory of the ground-state spin of the NV^{-} center in diamond. *Physical Review B* **2012,** *85* (20), 205203.
31. Mathur, N.; Mukherjee, A.; Gao, X.; Luo, J.; McCullian, B. A.; Li, T.; Vamivakas, A. N.; Fuchs, G. D., Excited-state spin-resonance spectroscopy of $\mathrm{V}_{\mathrm{B}}^{-}$ defect centers in hexagonal boron nitride. *Nature Communications* **2022,** *13* (1), 3233.
32. Blundo, E.; Surrente, A.; Spirito, D.; Pettinari, G.; Yildirim, T.; Chavarin, C. A.; Baldassarre, L.; Felici, M.; Polimeni, A., Vibrational Properties in Highly Strained Hexagonal Boron Nitride Bubbles. *Nano Letters* **2022,** *22* (4), 1525-1533.
33. Blundo, E.; Yildirim, T.; Pettinari, G.; Polimeni, A., Experimental Adhesion Energy in van der Waals Crystals and Heterostructures from Atomically Thin Bubbles. *Physical Review Letters* **2021,** *127* (4), 046101.
34. Yang, T.; Mendelson, N.; Li, C.; Gottscholl, A.; Scott, J.; Kianinia, M.; Dyakonov, V.; Toth, M.; Aharonovich, I., Spin defects in hexagonal boron nitride for strain sensing on nanopillar arrays. *Nanoscale* **2022,** *14* (13), 5239-5244.
35. Li, Z.; Lv, Y.; Ren, L.; Li, J.; Kong, L.; Zeng, Y.; Tao, Q.; Wu, R.; Ma, H.; Zhao, B.; Wang, D.; Dang, W.; Chen, K.; Liao, L.; Duan, X.; Duan, X.; Liu, Y., Efficient strain modulation of 2D materials via polymer encapsulation. *Nature Communications* **2020,** *11* (1), 1151.
36. Yang, W.; Yang, Y.; Zheng, F.; Zhang, P., Vibration responses of h-BN sheet to charge doping and external strain. *The Journal of Chemical Physics* **2013,** *139* (21), 214708.
37. Cai, Q.; Scullion, D.; Falin, A.; Watanabe, K.; Taniguchi, T.; Chen, Y.; Santos, E. J. G.; Li, L. H., Raman signature and phonon dispersion of atomically thin boron nitride. *Nanoscale* **2017,** *9* (9), 3059-3067.
38. Mennel, L.; Furchi, M. M.; Wachter, S.; Paur, M.; Polyushkin, D. K.; Mueller, T., Optical imaging of strain in two-dimensional crystals. *Nature Communications* **2018,** *9* (1), 516.
39. Yao, K.; Finney, N. R.; Zhang, J.; Moore, S. L.; Xian, L.; Tancogne-Dejean, N.; Liu, F.; Ardelean, J.; Xu, X.; Halbertal, D.; Watanabe, K.; Taniguchi, T.; Ochoa, H.; Asenjo-Garcia, A.; Zhu, X.; Basov, D. N.; Rubio, A.; Dean, C. R.; Hone, J.; Schuck, P. J., Enhanced tunable second harmonic generation from twistable interfaces and vertical superlattices in boron nitride homostructures. *Science Advances* **2021,** *7* (10), eabe8691.

40. Kim, S.; Fröch, J. E.; Gardner, A.; Li, C.; Aharonovich, I.; Solntsev, A. S., Second-harmonic generation in multilayer hexagonal boron nitride flakes. *Opt. Lett.* **2019,** *44* (23), 5792-5795.
41. Wang, Z.; Wang, Y. B.; Yin, J.; Tóvári, E.; Yang, Y.; Lin, L.; Holwill, M.; Birkbeck, J.; Perello, D. J.; Xu, S.; Zultak, J.; Gorbachev, R. V.; Kretinin, A. V.; Taniguchi, T.; Watanabe, K.; Morozov, S. V.; Anđelković, M.; Milovanović, S. P.; Covaci, L.; Peeters, F. M.; Mishchenko, A.; Geim, A. K.; Novoselov, K. S.; Fal'ko, V. I.; Knothe, A.; Woods, C. R., Composite super-moiré lattices in double-aligned graphene heterostructures. *Science Advances* **2019,** *5* (12), eaay8897.
42. Barson, M. S. J.; Peddibhotla, P.; Ovartchaiyapong, P.; Ganesan, K.; Taylor, R. L.; Gebert, M.; Mielens, Z.; Koslowski, B.; Simpson, D. A.; McGuinness, L. P.; McCallum, J.; Prawer, S.; Onoda, S.; Ohshima, T.; Bleszynski Jayich, A. C.; Jelezko, F.; Manson, N. B.; Doherty, M. W., Nanomechanical Sensing Using Spins in Diamond. *Nano Letters* **2017,** *17* (3), 1496-1503.